

Four-port photonic structures with mirror-time reversal symmetries

This content has been downloaded from IOPscience. Please scroll down to see the full text.

2016 New J. Phys. 18 075010

(<http://iopscience.iop.org/1367-2630/18/7/075010>)

View [the table of contents for this issue](#), or go to the [journal homepage](#) for more

Download details:

IP Address: 129.133.90.197

This content was downloaded on 22/05/2017 at 02:58

Please note that [terms and conditions apply](#).

You may also be interested in:

[Metamaterial, plasmonic and nanophotonic devices](#)

Francesco Monticone and Andrea Alù

[Optomechanical interactions in non-Hermitian photonic molecules](#)

D W Schönleber, A Eisfeld and R El-Ganainy

[\$\mathcal{P}\mathcal{T}\$ -symmetry breaking in the steady state of microscopic gain–loss systems](#)

Kosmas V Kepesidis, Thomas J Milburn, Julian Huber et al.

[Jamming anomaly in \$\mathcal{PT}\$ -symmetric systems](#)

I V Barashenkov, D A Zezyulin and V V Konotop

[Directional excitation without breaking reciprocity](#)

Hamidreza Ramezani, Marc Dubois, Yuan Wang et al.

[Relativistic Zitterbewegung in non-Hermitian photonic waveguide systems](#)

Guanglei Wang, Hongya Xu, Liang Huang et al.

[Transmission lines emulating moving media](#)

J Vehmas, S Hrabar and S Tretyakov

[Scattering properties of \$\mathcal{PT}\$ -symmetric layered periodic structures](#)

O V Shramkova and G P Tsironis



PAPER

Four-port photonic structures with mirror-time reversal symmetries

OPEN ACCESS

RECEIVED

16 March 2016

REVISED

21 June 2016

ACCEPTED FOR PUBLICATION

22 June 2016

PUBLISHED

12 July 2016

Original content from this work may be used under the terms of the [Creative Commons Attribution 3.0 licence](#).

Any further distribution of this work must maintain attribution to the author(s) and the title of the work, journal citation and DOI.

Huanan Li¹, Roney Thomas¹, F M Ellis and Tsampikos Kottos

Physics Department, Wesleyan University, Middletown, CT 06457, USA

¹ The first two authors contributed equally to this work.E-mail: tkottos@wesleyan.edu

Keywords: mirror-time reversal symmetry, isolation, four-port photonic structures

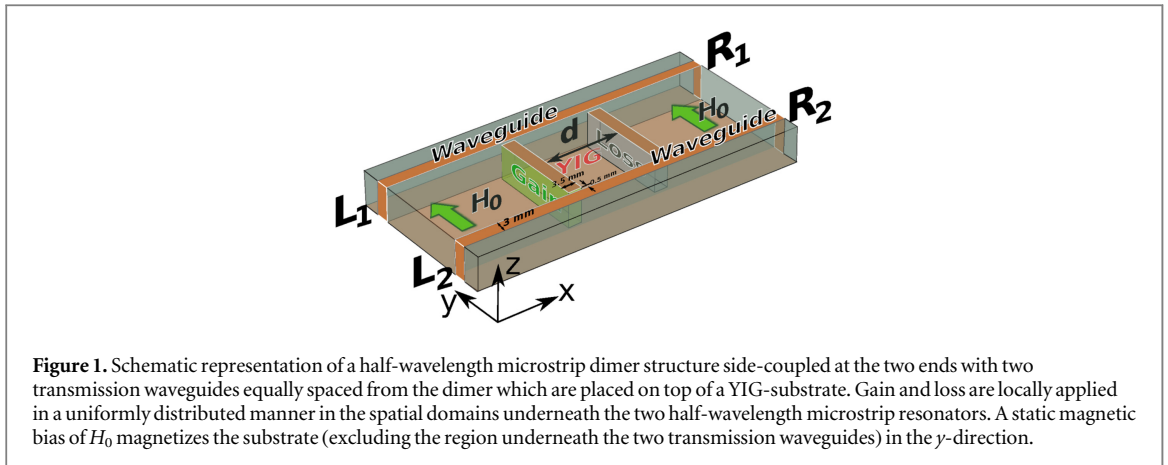
Abstract

We investigate the transport characteristics of a four-port gyrotropic photonic structure with mirror-time reversal symmetry. The structure consists of two coupled cavities with balanced amplification and attenuation. The cavities are placed on top of a gyrotropic substrate and are coupled to two bus waveguides. Using detail simulations in the microwave domain we demonstrate a strong non-reciprocal intra-guide port transport and an enhanced inter-guide port transmittance. The non-reciprocal features are dramatically amplified in the gain-loss parameter domain where an exceptional point degeneracy, for the associated isolated set-up, occurs. These results are explained theoretically in terms of an equivalent lumped circuit.

1. Introduction

Synthetic photonic structures with anti-linear symmetries have attracted a lot of attention during the last five years [1–20]. Due to the presence of appropriately tailored amplification and attenuation elements, they are described by non-Hermitian mathematical models which violate the time reversal symmetry \mathcal{T} . Nevertheless, these systems respect a joint antilinear symmetry \mathcal{ST} , where \mathcal{S} represents some linear operator associated with a spatial symmetry (e.g. parity, π -rotations, mirror symmetry etc). Typically the associated mathematical models also violate the \mathcal{S} -symmetry. The most prominent category are parity-time (\mathcal{PT}) symmetric systems, where the linear operator \mathcal{P} is associated with the parity. The invariance under \mathcal{PT} -symmetry imposes certain constraints on the spatial arrangement of the gain and loss elements. Specifically the index of refraction of a \mathcal{PT} -symmetric photonic system must satisfy the condition $n(r) = n^*(-r)$ [1, 2]. An obvious motivation for the investigation of \mathcal{PT} -symmetric structures is that they provide an excellent playground to study the effects of symmetries (and their violation) in a controllable laboratory environment [2–7]. But most importantly, it turned out that these systems can open new technological avenues for the manipulation of electromagnetic signals. Thus, phenomena like asymmetric transport [5, 6, 12–14], unidirectional invisibility [3, 4, 8], non-reciprocal Bloch oscillations [9, 10], control of lasing modes [6, 7], CPA-lasers [15, 21], lasing suppression via gain [17–19], unidirectional lasers [20] and hypersensitive sensors [22] are some of the new technological features associated with these type of structures.

Given the above success of \mathcal{PT} -symmetric photonic structures it is natural to extend the investigation into the more general family of \mathcal{ST} -symmetric systems. Of special interest is the case where magneto-optical effects, associated with a vector potential which cannot be gauged away, are involved [14, 20, 23, 24]. In this case the notion of time-reversal symmetry has to be adopted accordingly, i.e. it is not only associated with a simple conjugation $i \rightarrow -i$ but it also involves a change in the direction of the vector potential. The motivation to investigate this type of photonic structure is associated with the possibility to induce giant non-reciprocal effects—a theme of ongoing intense investigation [25–28]. Traditionally ferrite materials such as yttrium-iron garnet (YIG) are invoked in the design of photonic (both in the microwave and optical) non-reciprocal devices. The degree of non-reciprocity in any particular application is always a trade-off between the strength of the gyromagnetic coupling, losses associated with spin-wave relaxation, and the geometry of the wave-ferrite interaction.



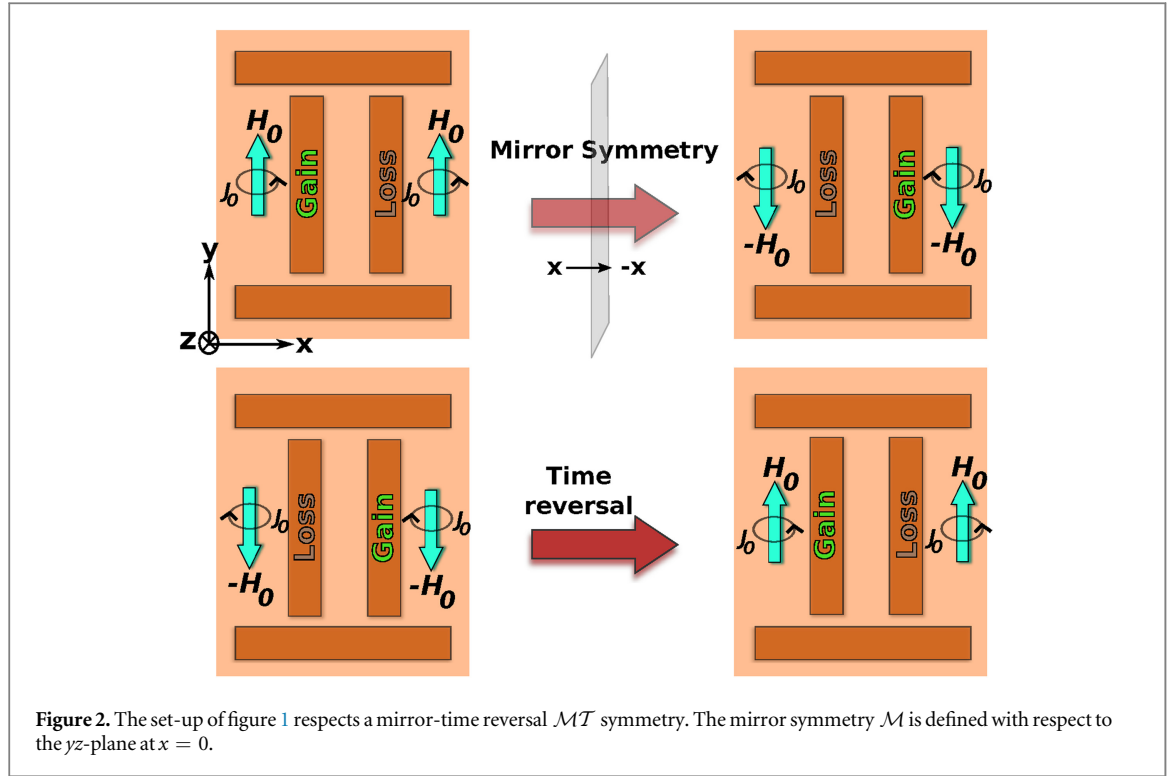
In this paper we analyze the transport characteristics of a four-port photonic structure with anti-linear mirror-time reversal (\mathcal{MT}) symmetries in the presence of magneto-optical effects. The structure consists of two \mathcal{MT} -symmetric cavities on a YIG substrate shown in figure 1. The cavities are coupled to two bus waveguides. We show that the whole structure possesses strong non-reciprocal behavior between left and right ports associated with the same waveguide (intra-guide ports) while it demonstrates an enhanced transmittivity, due to the active elements, between cross-ports of the two different waveguides (inter-guide ports). This behavior is strongly enhanced in the parameter domain where exceptional point (EP) degeneracies of the underlying isolated resonators occurs. The results are numerically demonstrated in the microwave domain and are accompanied by a thorough analytical study of a lumped circuit equivalent.

The organization of the paper is as follows. In the next section 2 we introduce the microwave photonic structure. A numerical analysis of the eigenmodes is reported in section 2.1 while in section 2.2 we report our numerical results for the transport properties of this system. In section 3 we present the lumped circuit analog and theoretically analyze its transport characteristics. Specifically in section 3.1, we present a general introduction to the lumped elements of an \mathcal{MT} symmetric system and their equivalence with the microwave components. In section 3.2 we present the lumped analog of the four-port microwave photonic structure. First we analyze the eigenmodes of the isolated set-up in section 3.3. In section 3.4 we analyze the properties of the scattering matrix of this system. Finally section 3.5 discuss the scattering properties of this system and demonstrate the universal nature of the non-reciprocal intra-guide transport in such set-ups. Our conclusions are given at the last section 4.

2. Microwave photonic structure

The microwave photonic structure that we consider, shown in figure 1, is the minimal four-port microstrip configuration capable of demonstrating \mathcal{MT} symmetric nonreciprocity. It consists of two transmission lines, each connected to a left and right port. A pair of proximity coupled half-wave resonators, referred to as the dimer, bridge the space between the waveguides. Small gaps end couple the dimer to each of the transmission lines, leading to a coupling between the two transmission line buses dominated by the dimer resonator. All of the microstrip structures lay on the top of a 8.75 mm thick YIG substrate, with relative permittivity $\epsilon_r = 15$ [29], and a ground plane below. The resonator dimer and the transmission waveguide traces are modeled in the thin, perfect conducting limit. The length of the microstrip resonators are chosen to be $l = 24.5$ mm long, supporting half-wavelength resonances of approximately $\omega/2\pi = 1.24$ GHz. The distance between the two microstrip resonators is $d = 20$ mm which correspond to a phase delay $\tilde{d} \equiv kd = 2.36$ rad. Later on in section 3.5 we discuss the role of the phase delay in our construction. The microstrip ends are separated by a 0.5 mm gap from the sides of the two 3 mm wide transmission lines.

The YIG-substrate is divided into two types: (i) active domains in the regions just underneath the two microstrip resonators, and (ii) a passive domain elsewhere (see figure 1). A balanced gain and loss is introduced in the two active regions by adding opposite imaginary parts to the YIG permittivity, $\epsilon_r = 15 \times (1 \pm i\alpha\gamma)$, to each resonator of the dimer. Here, γ is a parameter designating the strength of the balanced gain or loss defined so that each resonator, if isolated, would experience exponential growth or decay with $\gamma = |2 \text{Im}(\omega)/\text{Re}(\omega)|$. The parameter α is a numerically determined factor of (order unity for the configuration of figure 1) accounting for the precise geometrical configuration of the modified permittivity. Furthermore, the YIG-substrate is magnetized with a DC bias field H_0 along the y -axis, parallel to the resonator microstrips. The magnetic



permeability matrix $\hat{\mu}$ that describes the YIG takes the form:

$$\hat{\mu} = \mu_0 \begin{bmatrix} \mu_r & 0 & i\kappa_o \\ 0 & 1 & 0 \\ -i\kappa_o & 0 & \mu_r \end{bmatrix}; \mu_r = 1 + \kappa_o; \kappa_o = \frac{\omega\omega_m}{\omega_0^2 - \omega^2}, \quad (1)$$

where $\omega_0 = \mu_0\gamma_e H_0$ and $\omega_m = \mu_0\gamma_e M_s$, and we have neglected loss. Here, ω_0 corresponds to the precession frequency of an electron in the externally applied magnetic bias H_0 of 1600 Oe, and ω_m denotes the electron Larmor frequency at the saturation magnetization, $M_s = \frac{1750}{4\pi}$ G of the ferrite medium with gyromagnetic constant $\gamma_e = 1.76 \times 10^{11}$ rad sT⁻¹. Additionally, μ_0 and ω represent the permeability of free space and angular frequency of the radiation.

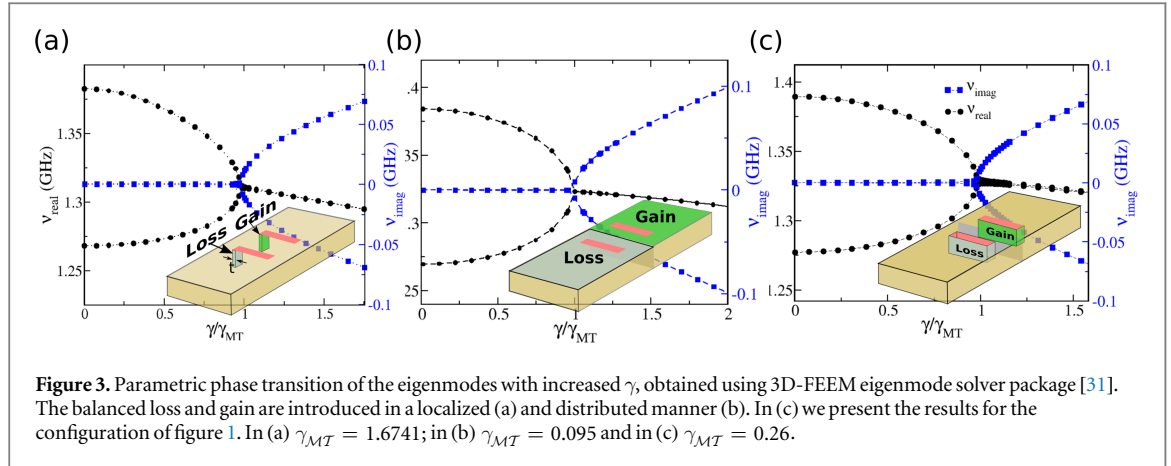
The structure shown in figure 1 respects an antilinear mirror-time reversal symmetry as is demonstrated in figure 2. The linear mirror-symmetry operator \mathcal{M} performs a reflection $(x, y, z) \rightarrow (-x, y, z)$ with respect to the mirror yz -plane at $x = 0$ and reverses the direction of the magnetic field $\vec{H}_0 \rightarrow -\vec{H}_0$. The antilinear time-reversal operator \mathcal{T} , performs a complex conjugation $i \rightarrow -i$ together with an inversion of the direction of the magnetic vectors i.e. $\vec{H}_0 \rightarrow -\vec{H}_0$. In the specific case of gain and loss elements the complex conjugation operation is equivalent to the exchange of the gain and loss elements.

2.1. Eigenmode analysis of the isolated system

We start our analysis with the parametric evolution of the eigenfrequencies of the isolated dimer associated with the photonic set-up of figure 1.

A novel feature of non-Hermitian systems with antilinear symmetries, is the possibility to possess an entirely real spectrum for some values of the gain/loss parameter γ [30]. In this parameter domain, coined exact phase, the eigenmodes are invariant under the antilinear operator. As the gain/loss parameter γ , increases beyond some critical value $\gamma > \gamma_{\mathcal{MT}}$, the spectrum becomes partially or completely complex and the system enters the so-called broken phase. In this domain the eigenmodes do not respect the antilinear symmetry—although the system itself remains invariant under \mathcal{MT} . At $\gamma = \gamma_{\mathcal{MT}}$ the eigenfrequencies and the associated eigenmodes coalesce and the system experiences an EP degeneracy.

We investigate the \mathcal{MT} -symmetry phase transition for the set-up of figure 1 with the bus waveguides removed (see insets of figure 3). We refer to this as the isolated configuration. Using the 3D-finite element electromagnetic (FEEM) eigenfrequency simulation package of COMSOL [31] we explore the \mathcal{MT} -symmetry phase transition for three scenarios associated with the distribution of the gain and loss media (the modified permittivity) beneath the microstrips: (i) the gain and loss are collapsed into a localized patch at the resonator ends, as shown schematically in the inset of figure 3(a); (ii) the gain and loss is uniformly distributed over the left and right sides of the whole YIG-substrate, as shown in figure 3(b); and; (iii) finally, the case originally described



in figure 1 where the gain and loss is confined directly beneath the individual resonator striplines is reported in figure 3(c).

The purpose of the analysis of these isolated system scenarios is to demonstrate that the MT -symmetric behavior is only weakly dependent on the details of how the gain and loss is actually achieved. While the latter two scenarios could be realized in the optics framework by appropriately distributed gain and loss media, case (i) is more relevant to the microwave domain. Concentrating the gain and loss into a small patch at the anti-nodes of the half-wave electric potential oscillations in the microstrip resonator mimics the action of discrete electronic gain or loss elements such as transistors or resistors [21, 32]. In all cases, the geometric parameter α is calibrated to preserve the stated meaning of the gain/loss parameter γ .

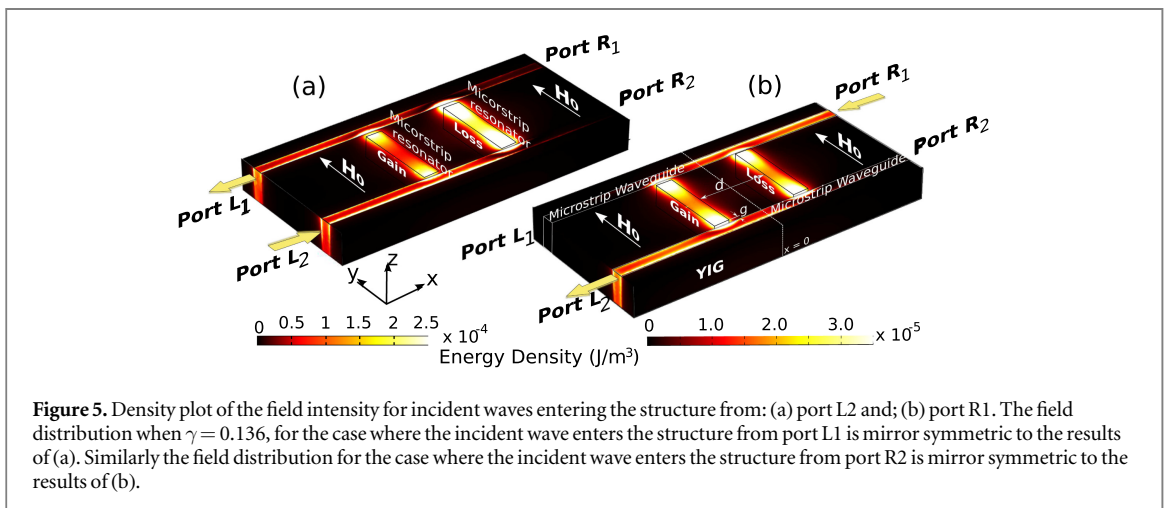
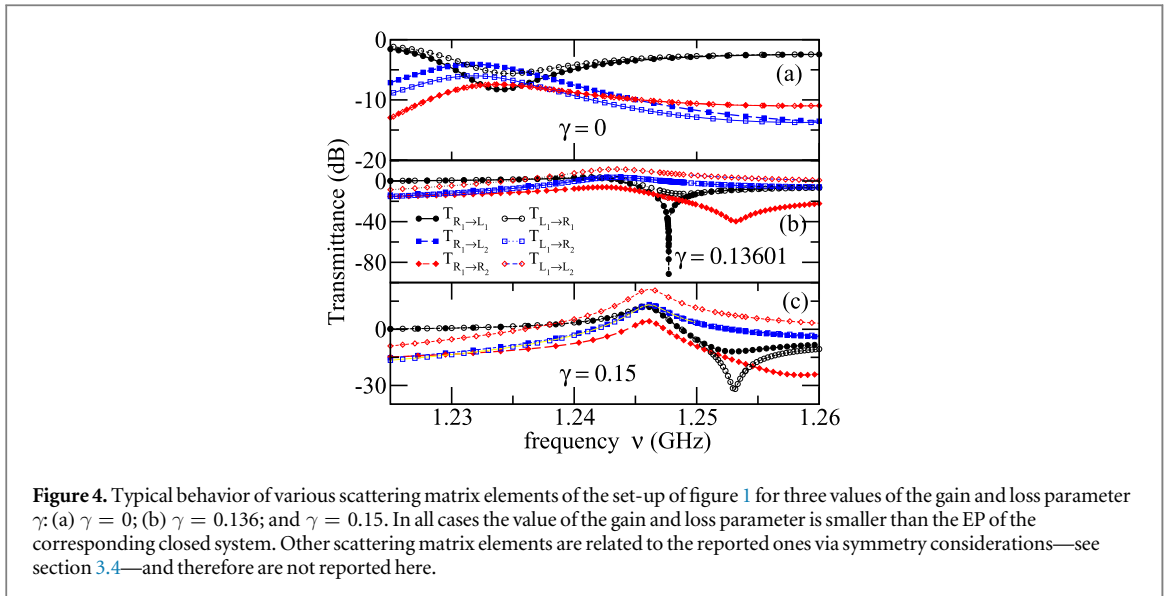
Figure 3 illustrates the parametric evolution of the isolated eigenfrequencies as a function of the gain/loss parameter. When $\gamma = 0$, the coupled microstrip resonators support two low order resonant modes: a symmetric (low frequency) and an antisymmetric (higher frequency) modes defined by the parallel and anti-parallel directional flow of the surface currents in the striplines. For $\gamma = 0$ the associated eigenfrequencies have a small and similar imaginary value due to a weak radiative loss to the simulation boundaries. As γ increases the real part of the eigenfrequencies of the modes changes (see figures 3(a)–(c)) while the associated imaginary part remains the same. At some critical value of the gain/loss parameter $\gamma = \gamma_{MT}$, the eigenvalues coalesce and a spontaneous MT -symmetric phase transition occurs. For $\gamma > \gamma_{MT}$ the real part of the eigenfrequencies remains degenerate while their imaginary part bifurcates to two distinct values of opposite sign. The eigenmodes take on a left/right flavor with the gain side exponentially growing in time, and the loss side exponentially decaying in time. The main results in this figure show that the quantitative behavior of the three set-ups (i)–(iii) is the same and does not depend on the details of how gain and loss are introduced into the system. For the remainder of the simulations of the non-isolated system, we will restrict analysis to the case (iii), where gain and loss are confined to be below the individual resonator microstrips.

2.2. Transport properties

Next we turn to the analysis of the transport characteristics of the four-port system of figure 1. The structure is simulated with COMSOL's 3D FEEM numerical software. A mesh density with element size of $\lambda/8$ within the active domains underneath the two microstrips and $\lambda/4$ in the surrounding bulk YIG-substrate was used, and confirmed for accuracy, where λ is the wavelength inside the medium. Quasi-TEM waves are introduced or collected from the device transmission lines via impedance-matched ports, supplied through the COMSOL software, defined between the edge of the microstrip waveguide and ground plane. An example of the frequency dependence of the scattering matrix elements is shown in figure 4 for three values of the gain and loss parameter γ . For intermediate values of γ we observe a strong non-reciprocal effect for intra-guide transmittance while the inter-guide transmittance is enhanced. A density plot of the propagating electromagnetic field for the value of γ where this effect is observed, is reported in figure 5. Below we further analyze this behavior².

Numerical simulations were carried out to quantify the dependence of the scattering coefficients between various ports as a function of increasing gain–loss parameter. We report only the transmitted signals with incident wave entering the structure from port R_1 and/or port L_1 . All other transmitted coefficients (and also reflections to the incident ports) are related with the reported transmittances via symmetry considerations, see section 3.4. For example $T_{L_1 \rightarrow R_2} = T_{L_2 \rightarrow R_1}$ etc. An impressive conclusion of our analysis is the fact that for some

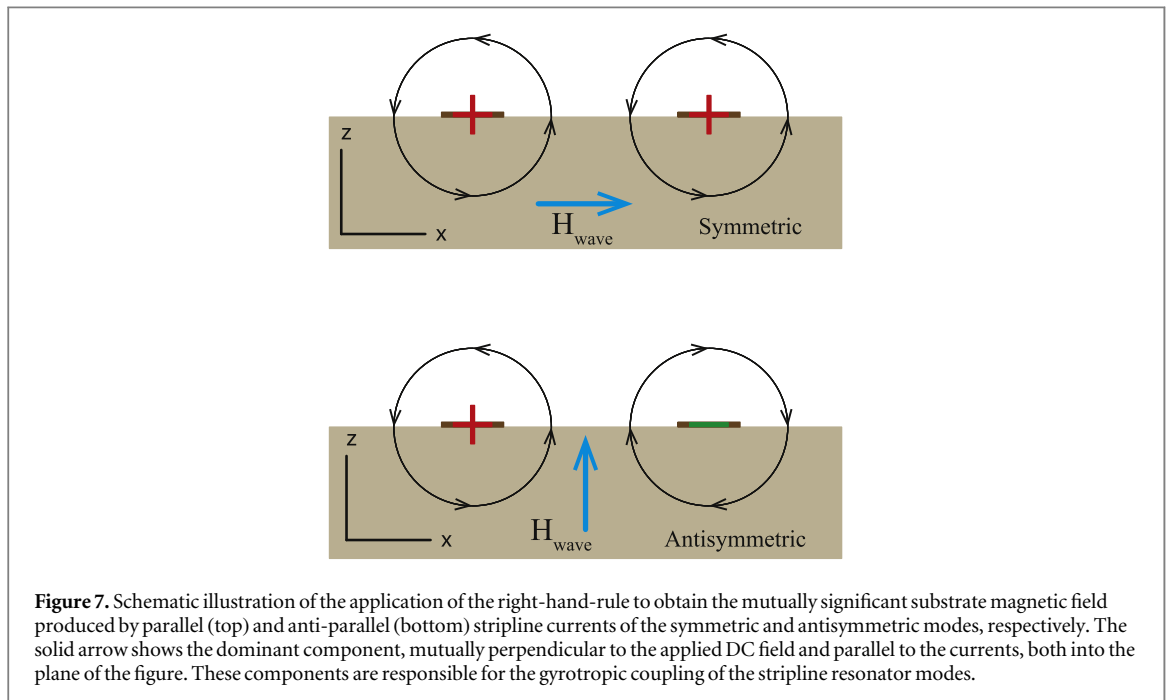
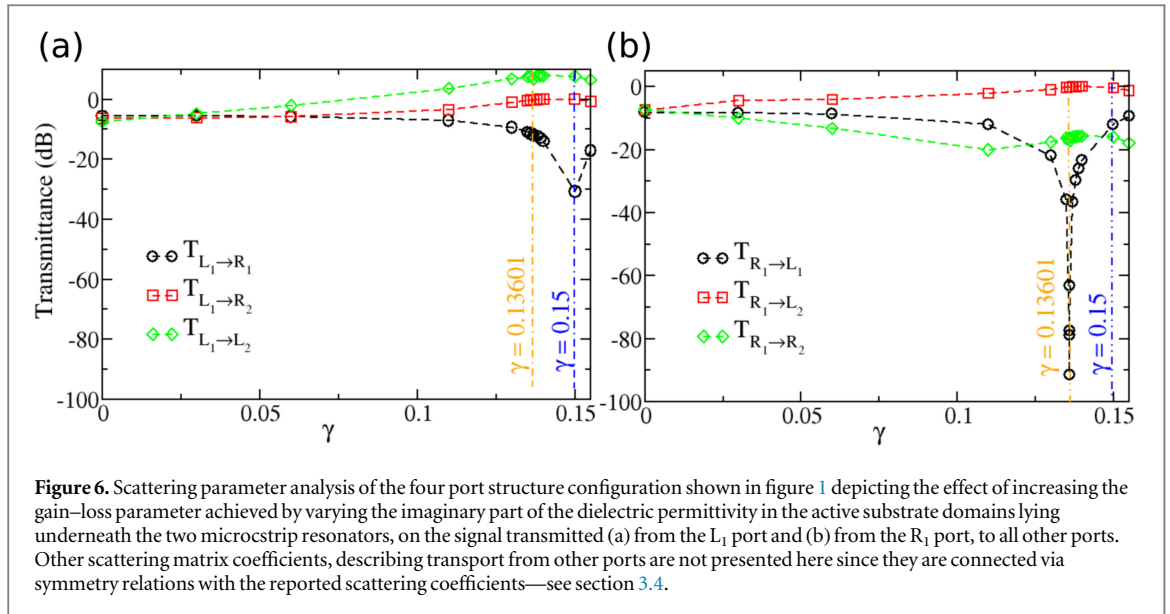
² We restrict all of the following discussion in the frequency regime near the symmetric mode where the transmission of waves through the system shows a maximum non-reciprocity.



critical value of the gain–loss parameter ($\gamma = 0.13601$) a giant isolation of the L_1 port from the signal transmitted from the R_1 port is achieved (i.e. $T_{R_1 \rightarrow L_1} \sim -90$ dB or essentially zero) while at the same time we have a healthy signal that is radiated towards the L_2 port ($T_{R_1 \rightarrow L_2} \sim -0.2$ dB). The signal transmitted from port L_1 to port R_2 , is $T_{L_1 \rightarrow R_2} \sim -0.2$ dBs while we have also a healthy signal from L_1 to L_2 ports, $T_{L_1 \rightarrow L_2} \sim 7$ dBs. We finally note that a non-reciprocal intra-guide behavior can occur for another value of $\gamma = 0.15$. However the phenomenon here is not as dramatic as previously. Below we proceed with a qualitative explanation of this strong intra-guide non-reciprocal effect, while in sections 3.4 and 3.5 we provide a detail theoretical explanation based on equivalences with a lumped circuit.

The nonreciprocity shown in figure 6 has its roots in the different propagation constant for circularly polarized waves travelling parallel to a static magnetic field exhibited in an otherwise isotropic magnetic medium. The question here is how can this difference be used to achieve a nonreciprocal transmission, and under which conditions the \mathcal{MT} -symmetry enhance the isolation? A classic ferrite-based nonreciprocal device needs to (1) create a circular polarization containing magnetic fields rotating perpendicular to the static bias magnetic field, and (2) allow separate components of the chiral wave to travel along paths that interfere upon recombination. The rotating field components couple differently to the spin precession of the magnetized ferrite, and experience a resulting phase difference. The structure of this four port device includes all of these features in its design.

Although there is not any obvious circular polarization, the symmetric and antisymmetric modes of the resonator dimer allow the equivalent to occur. Quasi-TEM waves on a single microstrip have only one polarization defined by the single mode, but a pair of parallel striplines, having two components, can result in two independent magnetic fields. These wave fields, perpendicular to the static field, also include components perpendicular to each other, the necessary condition for the gyromagnetic coupling. The symmetric mode, with



parallel stripline currents, is dominated by a mutual substrate magnetic field parallel to the plane of the substrate. The antisymmetric mode, with anti-parallel currents, is dominated by a mutual substrate magnetic field perpendicular to the plane of the substrate. Figure 7 schematically illustrates the application of the right-hand-rule to the region of the substrate significantly influenced by the current-induced fields of both modes.

The rotating field requirement imposes further conditions on the resonances. The fields of figure 7 need to be excited simultaneously. Normally this would be difficult to achieve since the two modes are split by non-gyrotropic coupling. However, the symmetry of the transmission line coupling helps in this respect. Depending on the path delay of the resonator coupling to the transmission lines, resonant mode and the off-resonant mode can have different effective coupling strengths to the wave excitation in the waveguide. For example, the resonant mode could be weakly coupled, and the off-resonant mode could be strongly coupled, resulting in a more balanced excitation of both modes by the same frequency. Another rotating field requirement is that there be a quadrature phase difference between the two modes of figure 7. Without dissipation, symmetry of the structure prevents such a phase delay: the resonances are either in-phase, or out of phase, with the effective drive. However, a resonant quadrature phase relationship will be introduced by any small dissipation, usually naturally occurring, that assures some finite bandwidth while passing through the quadrature condition. The second

non-reciprocity requirement that there is a path-length difference, is available through both the phase delay associated with the spatial separation of the end coupling to the resonator elements, and as an inherent ‘dwell time’ of a resonator.

It is now clear why the non-reciprocity could be enhanced by the \mathcal{MT} symmetric behavior. As the gain/loss parameter γ progresses toward the EP, $\gamma_{\mathcal{MT}}$, both the frequencies of the modes and their phases coalesce. The novel eigenfrequency and eigenmode behavior present in these systems introduces a new parameter distinctly capable of tuning the device in unusual ways to enable the gyrotropic coupling.

The next section discusses these features in the context of the simpler lumped-element model containing only the essential parameters.

3. Lumped circuitry analog

3.1. Lumped elements

The configuration simulated in section 2 consisted of the active, gyromagnetically coupled microstrip dimer coupled to the two microstrip transmission lines making up the ports. As simple as this system is, the subtlety of the physical coupling between the microstrip elements and the mode structure of the coupled resonators required the COMSOL analysis for an accurate prediction of the device behavior. A more intuitive approach that naturally leads to a theoretical analysis is the lumped element electronic analog. Here, the resonator pair with its inter-resonator coupling and gain/loss character are replaced by appropriately coupled LC circuits. All spatial symmetry considerations, with the exception of the phase delay associated with the microstrip sections between the resonator ends, can be reduced to a matter of network topology defined through the application of Kirchoff’s laws to fundamental electronic elements. Physical symmetry is reduced to the circuit network as defined by its node topology with appropriately valued connecting elements. The parity, mirror, and time reversal operations are equivalent to the interchange of labels corresponding to pairwise associated circuit nodes, with proper consideration of the resistive and gyrotropic elements through a sign change.

Resistors change their sign upon time-reversal, where negative resistance represents the simplest conceptual inclusion of amplification into electronics. Dissipative loss turns into gain and Kirchoff’s laws can be used without modification subject to a condition described below. Experimentally, negative resistance can easily be implemented with negative impedance converters but can only approximate the ideal due to inherent limitations of the required amplifying components [21].

Analysis of circuits including negative resistance elements, however, requires respecting a subtle condition: any two terminal circuit structure reducing to a pure negative resistance will be undefined unless the structure is placed in parallel with a capacitance. This conclusion results from the divergence of the pole associated with parallel RC_p combinations (with $R < 0$) in the limit of $C_p \rightarrow 0$. The pole with the usual positive resistance has a sign that corresponds to exponential decay and therefore has a physically valid limit as $C_p \rightarrow 0$. For example, the solution for the standard series LRC circuit, though it appears to have a mathematically appropriate solution for negative R , is non-physical in that realm: the hidden pole corresponds to an exponentially growing solution with a diverging rate as $C_p \rightarrow 0$. The parallel LRC configuration with $R > 0$ is not subject to this oversight.

The gyrotropic nature of the biased magnetic substrate beneath the microstrip resonator dimer is included electronically by the gyrator, shown schematically in figure 8 and defined by its conductance matrix, with G_0 being the strength of the gyration

$$\begin{pmatrix} i_1 \\ i_2 \end{pmatrix} = \begin{pmatrix} 0 & G_0 \\ -G_0 & 0 \end{pmatrix} \begin{pmatrix} v_1 \\ v_2 \end{pmatrix}. \quad (2)$$

Although as an actual device, the ideal gyrator can only be approximately implemented in the microwave regime, we nevertheless include it for its conceptual simplicity in allowing a lumped model for the substrate mediated interaction. The mirror operation applied to this device changes the sign of G_0 .

Thus, for a \mathcal{MT} -symmetric circuit incorporating these basic elements, it is necessary that (1) all reactive elements either have representation in parity-associated network pairs, or directly connect parity inverted network nodes, (2) all Ohmic elements are paired with opposite sign, and (3) each negative Ohmic element has an associated parallel capacitance, or AC equivalent, as part of the circuit. Valid \mathcal{MT} -circuits of arbitrary complexity can be built up using these simple rules, though their stability needs to be independently determined.

3.2. Electronic analog circuit

Figure 9(a) shows the \mathcal{MT} -symmetric lumped element circuit used to simplify the four-port microstrip device simulated in COMSOL. The microstrip resonator pair is replaced by a pair of LC resonators, with the left side experiencing a gain, and the right side experiencing a loss of equivalent magnitude represented as respective negative and positive parallel resistances of magnitude R . The original microstrip resonators experience both

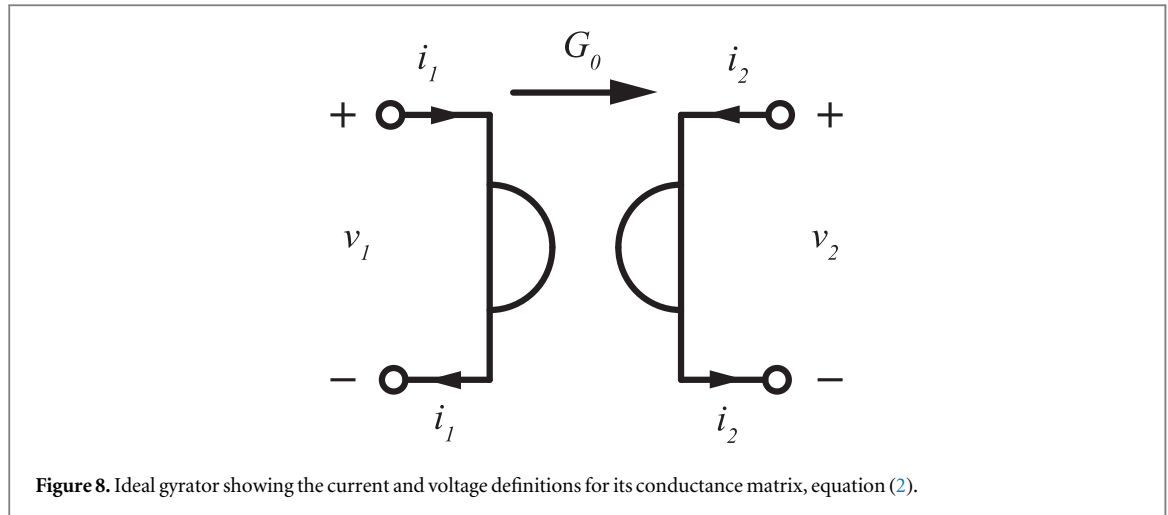


Figure 8. Ideal gyrator showing the current and voltage definitions for its conductance matrix, equation (2).

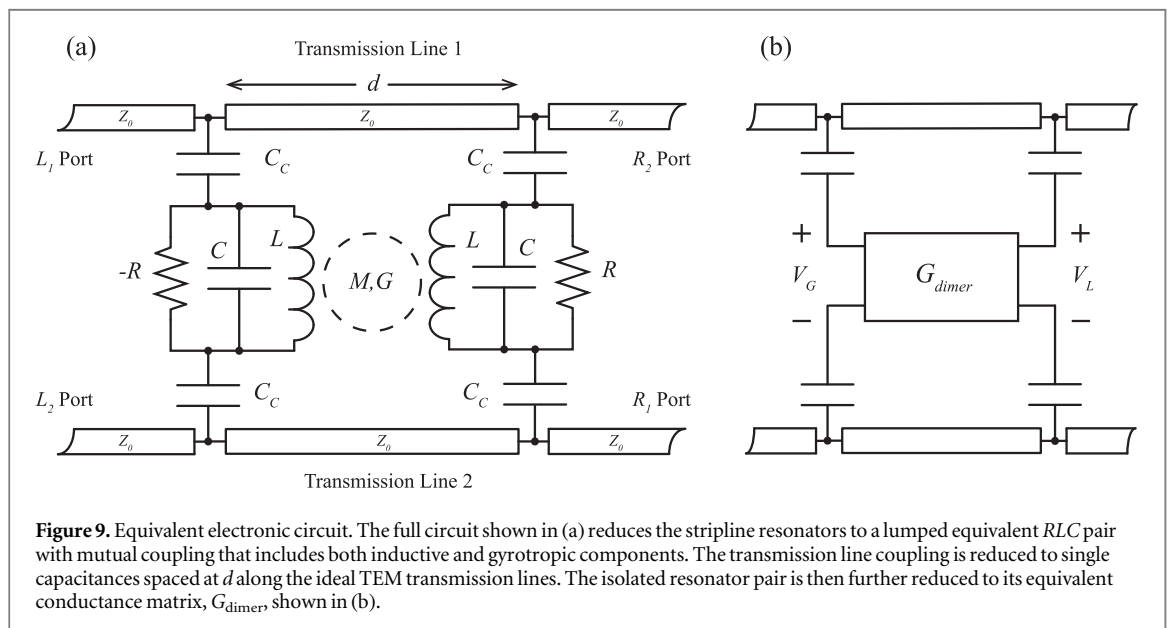


Figure 9. Equivalent electronic circuit. The full circuit shown in (a) reduces the stripline resonators to a lumped equivalent RLC pair with mutual coupling that includes both inductive and gyrotropic components. The transmission line coupling is reduced to single capacitances spaced at d along the ideal TEM transmission lines. The isolated resonator pair is then further reduced to its equivalent conductance matrix, G_{dimer} , shown in (b).

capacitive and inductive coupling due to their proximity, and a gyration component arising from the biased magnetic substrate. The lumped element resonator coupling is limited to mutual inductance, which captures the proper mode splitting of the quasi-TEM proximity coupling, and a pure gyration component.

The resonators are capacitively coupled by C_c to points along an ideal TEM transmission line, separated by a length d . The transmission lines with impedance Z_0 are then continued on to the device ports, which in this lumped model, are collapsed to the respective nodes of figure 9. Realistic values for the lumped components can be chosen to match the observed resonances of the COMSOL simulation.

This model, with the resonator section limited to the four parallel nodes of the LC resonator pair, provides for a convenient separation of the complete dimer into a generic conductance matrix, G_{dimer} , as illustrated in figure 9(b). This separation not only simplifies the expression of Kirchhoff's laws for the complete system, but also simplifies the analysis of the isolated dimer described by the solutions of $G_{dimer} V = 0$ with

$$G_{dimer} = \frac{\begin{pmatrix} 1 & 0 \\ 0 & 1 \end{pmatrix}}{Z_{\text{reac}}(\omega)} + \begin{pmatrix} -\frac{1}{R_1} & 0 \\ 0 & \frac{1}{R_2} \end{pmatrix} + \frac{\begin{pmatrix} \mu^2 & -\mu \\ -\mu & \mu^2 \end{pmatrix}}{i\omega L(1 - \mu^2)} + G_0 \begin{pmatrix} 0 & 1 \\ -1 & 0 \end{pmatrix}, \quad (3)$$

where $V = \begin{pmatrix} V_g \\ V_l \end{pmatrix}$ with the entries V_g and V_l denoting the voltage across the gain side and the loss side of the dimer, as illustrated in figure 9. In the first term of equation (3), $Z_{\text{reac}}(\omega)^{-1} = i\omega C + (i\omega L)^{-1}$ is the conductance of the individual parallel LC resonators, while the second term gives the negative and positive conductances associated with gain and loss sides, which in general might not be exactly balanced. The third and fourth terms

express strength of the inter-resonator coupling, given as the equivalent conductances associated with mutual-inductance $M = \mu L$ and the gyration, respectively.

Kirchoff's laws for the dimer including only this mutual inductance and gyration coupling between the oscillators are simplified by scaling the frequency and conductance by the bare LC natural frequency $\omega_0 = 1/\sqrt{LC}$, giving $DV = 0$ with

$$D \equiv \begin{bmatrix} -\gamma + i\tilde{\omega} + \frac{1}{i\tilde{\omega}(1-\mu^2)} & g - \frac{\mu}{i\tilde{\omega}(1-\mu^2)} \\ -g - \frac{\mu}{i\tilde{\omega}(1-\mu^2)} & \gamma + i\tilde{\omega} + \frac{1}{i\tilde{\omega}(1-\mu^2)} \end{bmatrix} + \gamma_0 I_2, \quad (4)$$

where the scaled conductance matrix D has been separated into an MT symmetric part with balanced gain/loss parameter γ and a small unbalanced intrinsic loss γ_0 satisfying $\gamma_0 - \gamma = -\frac{1}{R_1} \sqrt{\frac{L}{C}}$ and $\gamma_0 + \gamma = \frac{1}{R_2} \sqrt{\frac{L}{C}}$. The scaled gyration strength is $g = G_0 \sqrt{\frac{L}{C}}$, the scaled frequency is $\tilde{\omega} = \omega/\omega_0$, and I_2 is the identity matrix.

3.3. Eigenmode analysis

First we discuss the normal modes of the isolated balanced dimer by setting $\gamma_0 = 0$. The structure of that part of equation (4) implies relatively simple forms for the eigenvalues and eigenvectors. Respecting this structure indeed leads to a tractable form for the eigenvalue equation

$$\left(\tilde{\omega}^2 - \frac{1}{1-\mu}\right)\left(\tilde{\omega}^2 - \frac{1}{1+\mu}\right) - (g^2 - \gamma^2)\tilde{\omega}^2 = 0 \quad (5)$$

with eigenvalues of the antisymmetric and symmetric modes

$$\tilde{\omega}_{a/s}^0(\gamma) = \frac{\sqrt{\gamma_c^2 - \gamma^2} \pm \sqrt{\gamma_{MT}^2 - \gamma^2}}{2} \quad (6)$$

along with their redundant negatives, which are defined in terms of two critical points for the gain/loss parameter, *i. e.*, the MT symmetry breaking point

$$\gamma_{MT} = \sqrt{g^2 + \left[\sqrt{\frac{1}{1+\mu}} - \sqrt{\frac{1}{1-\mu}}\right]^2} \quad (7)$$

and an upper critical point

$$\gamma_c = \sqrt{g^2 + \left[\sqrt{\frac{1}{1+\mu}} + \sqrt{\frac{1}{1-\mu}}\right]^2}. \quad (8)$$

Note that the given forms explicitly show all of the relationships among the analogous EPs and the real and imaginary parts of the frequencies. The exact phase below the symmetry breaking point, $0 < \gamma < \gamma_{MT}$, is characterized by two purely real eigenfrequencies, while in the broken phase between this and the upper critical point, $\gamma_{MT} < \gamma < \gamma_c$ there is one real frequency with two opposite imaginary parts, and above γ_c , four pure imaginary frequencies. The opposite imaginary parts impose at least one exponentially growing mode above γ_{MT} making the isolated dimer unstable and inappropriate for consideration of steady-state behavior.

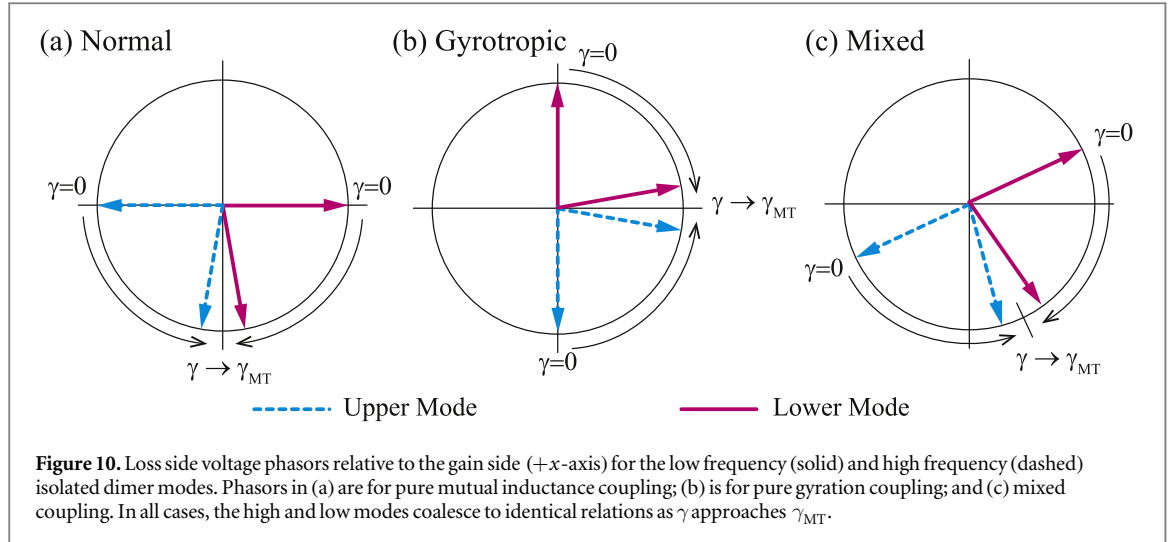
The normal modes in the exact phase are characterized by equal magnitudes for the voltage oscillations in the gain and loss sides, which are given by

$$\begin{pmatrix} V_g \\ V_l \end{pmatrix}_{a/s} = \frac{1}{\sqrt{2}} \begin{pmatrix} 1 \\ \exp(i\phi_{a/s}) \end{pmatrix} \quad (9)$$

with a phase $\phi_{a/s}$ of the loss side relative to the gain side of

$$\phi_{a/s} = \arg\left(\left(\frac{1}{1-\mu^2} - (\tilde{\omega}_{a/s}^0)^2 - i\gamma\tilde{\omega}_{a/s}^0\right)\left(\frac{\mu}{1-\mu^2} + ig\tilde{\omega}_{a/s}^0\right)\right). \quad (10)$$

As the gain/loss parameter traverses the exact region, $0 \leq \gamma \leq \gamma_{MT}$, the phase progresses from the in- and out-of-phase configuration of a Hamiltonian coupled oscillator pair, to a mode coalescence at γ_{MT} with a real frequency $\tilde{\omega}_a^0 = \tilde{\omega}_s^0 = (1-\mu^2)^{-1/4}$, where both the magnitudes and phases of the voltage oscillations are identical. The role of the gyration strength g is subtle: it acts in an orthogonal sense to the mutual inductance coupling because of its inherent non-reciprocal coupling of current and voltage, and results in mode phases initially related by $\pi/2$ usually indicative of dissipation. However, in spite of the gyration being characterized by a real conductance, it is actually a non-dissipative element. Figure 10 schematically illustrates the evolution of



the left and right voltage mode phasers for pure mutual inductance coupling in (a); pure gyration coupling in (b); and a combination of the two in (c). In all cases, the high and low mode coalesce as γ increases, approaching γ_{MT} .

We note that the gyration is thus imposing a normal mode character to the electronic circuit analogous to the circularly polarized eigenstates of free electromagnetic waves in the gyromagnetic medium of the device substrate. The combination of the gyrotropic coupling with normal reactive coupling allow the simple electronic circuit to embody all of the important features of the more nuanced microstrip dimer.

Now we impose the small unbalanced intrinsic loss, γ_0 of equation (4), into the system to generically account for losses in any real system. Specifically, up to $O(\gamma_0)$, the eigenfrequencies of the isolated symmetric and antisymmetric modes pick up nearly equal imaginary parts

$$\tilde{\omega}_s = \tilde{\omega}_s^0 + \eta_s \gamma_0, \quad (11)$$

$$\tilde{\omega}_a = \tilde{\omega}_a^0 + \eta_a \gamma_0, \quad (12)$$

$$\eta_s \approx \eta_a \approx \bar{\eta} \equiv \frac{\eta_s + \eta_a}{2} = \frac{1}{2}.$$

The closed system consisting of the nearly \mathcal{MT} -symmetric couples oscillators has now been modified by the parameter γ_0 to include a small unbalanced intrinsic loss common to both the symmetric and antisymmetric modes.

3.4. Scattering set-up

The full device circuit can now be considered by expressing the transmission lines, characterized by their impedance Z_0 and phase velocity v_p , as capacitively coupled to the circuit defined by the conductance matrix G_{dimer} , illustrated earlier in figure 9(b) and explicitly expressed in equation (4). The scaled coupling capacitances, $c = \frac{C_c}{C}$ are spaced at a scaled distance $\tilde{d} = \frac{d}{v_p \sqrt{LC}}$ along the respective transmission lines. Kirchoff's laws can now be rewritten in the framework of coupled-mode theory, expressing relations among the port wave components required to match the conductance terminal currents of G_{dimer}

$$\left(\zeta_0 LD + \frac{1}{2} C_m \right) V = C_m L (V_1^{\text{in}} - V_2^{\text{in}}), \quad (13)$$

$$V_1^{\text{out}} = -\zeta_0 LDV + PV_1^{\text{in}}, \quad (14)$$

$$V_2^{\text{out}} = \zeta_0 LDV + PV_2^{\text{in}}. \quad (15)$$

Here $C_m = \left(\frac{L^{-1}}{i\omega\epsilon\zeta_0} + I_2 \right)^{-1}$, $L = \frac{1}{2}(P + I_2)$ and $P = \begin{bmatrix} 0 & e^{-i\omega\tilde{d}} \\ e^{-i\omega\tilde{d}} & 0 \end{bmatrix}$ are 2×2 matrices resulting from the reduction of Kirchoff's laws with $\zeta_0 = Z_0 \sqrt{\frac{C}{L}}$. The incoming and outgoing port wave components for the upper transmission line (#1 of figure 9), $V_1^{\text{in}} = \begin{pmatrix} V_{L1}^+ \\ V_{R1}^- \end{pmatrix}$ and $V_1^{\text{out}} = \begin{pmatrix} V_{L1}^- \\ V_{R1}^+ \end{pmatrix}$ respectively, consist of forward (+) and backward (-) traveling wave voltage amplitudes at the left (L_1) and right (R_1) ports, which for this lumped

model are shortened to the connection nodes. Similarly, $V_2^{\text{in}} = \begin{pmatrix} V_{L2}^+ \\ V_{R2}^- \end{pmatrix}$ and $V_2^{\text{out}} = \begin{pmatrix} V_{L2}^- \\ V_{R2}^+ \end{pmatrix}$ refer to the corresponding components for the lower transmission line (#2 of figure 9).

Using the coupled-mode equations (13)–(15), one can get the relations between the outgoing signals and incoming signals, which defines a 4×4 scattering matrix S with block elements

$$\begin{aligned} S_{11}^{\text{oi}} = S_{22}^{\text{oi}} &= P - \left(C_m^{-1} + \frac{1}{2}(\zeta_0 LD)^{-1} \right)^{-1} L \\ S_{12}^{\text{oi}} = S_{21}^{\text{oi}} &= \left(C_m^{-1} + \frac{1}{2}(\zeta_0 LD)^{-1} \right)^{-1} L \end{aligned} \quad (16)$$

individually defined as

$$V_1^{\text{out}} = S_{11}^{\text{oi}} V_1^{\text{in}} + S_{12}^{\text{oi}} V_2^{\text{in}}, \quad (17)$$

$$V_2^{\text{out}} = S_{21}^{\text{oi}} V_1^{\text{in}} + S_{22}^{\text{oi}} V_2^{\text{in}}. \quad (18)$$

Furthermore, using equation (16) together with the definition of the P -matrix we can show that $|S_{m,m}^{\text{oi}}(n, n)|^2 = |S_{\bar{m},\bar{m}}^{\text{oi}}(n, n)|^2$ where $m, n = 1, 2$ and $\bar{m} = m - \delta_{m,2}$. We note that this relation connects the reflectance $|S_{m,m}^{\text{oi}}(n, n)|^2$ at a specific port to one of the transmittances to another port $|S_{\bar{m},\bar{m}}^{\text{oi}}(n, n)|^2$. In the special case where intrinsic losses are absent, i.e. $\gamma_0 = 0$, it is easy to show from the above equations that the scattering matrix S satisfies the following symmetry relation:

$$S^{-1}(\omega, \vec{H}) = \mathcal{M}TS(\omega, \vec{H})\mathcal{M}T = \begin{pmatrix} \sigma_x & 0 \\ 0 & \sigma_x \end{pmatrix} S^*(\omega, \vec{H}) \begin{pmatrix} \sigma_x & 0 \\ 0 & \sigma_x \end{pmatrix}, \quad (19)$$

$$\mathcal{M} = \begin{pmatrix} \sigma_x & 0 \\ 0 & \sigma_x \end{pmatrix} \cdot \hat{\Theta}, \quad (20)$$

where \mathcal{T} is the time reversal symmetry operator as it was defined previously in the presence of magnetic elements and \mathcal{M} is the mirror symmetry operator. The operator $\hat{\Theta}$ involved in the definition of the mirror symmetry reverses the direction of the magnetic field $\vec{H}_0 \rightarrow -\vec{H}_0$ while σ_x is the Pauli matrix.

Transmission and reflection coefficients are extracted from the elements $S_{ij}^{\text{oi}}(m, n)$, where $i = 1, 2$ and $j = 1, 2$ designate the top (1) or bottom (2) transmission lines, and $m = 1, 2$ and $n = 1, 2$ designate the left (1) or right (2) ports. For example, the reflection coefficient from the right port of the bottom transmission line would be $\mathcal{R}_{R_2} = |S_{22}^{\text{oi}}(2,2)|^2$ and the transmission from that port to the left port of the top transmission line would be $\mathcal{T}_{R_2 \rightarrow L_1} = |S_{12}^{\text{oi}}(1,2)|^2$.

To quantify the isolation effect for the signal between any pair of ports we introduce an associated nonreciprocity parameter, NR, measured in dB. For example,

$$\text{NR}(\gamma) = 10 \times \max_{\omega} \left\{ \left| \log_{10} \frac{\mathcal{T}_{R_1 \rightarrow L_1}}{\mathcal{T}_{L_1 \rightarrow R_1}} \right| \right\}, \quad (21)$$

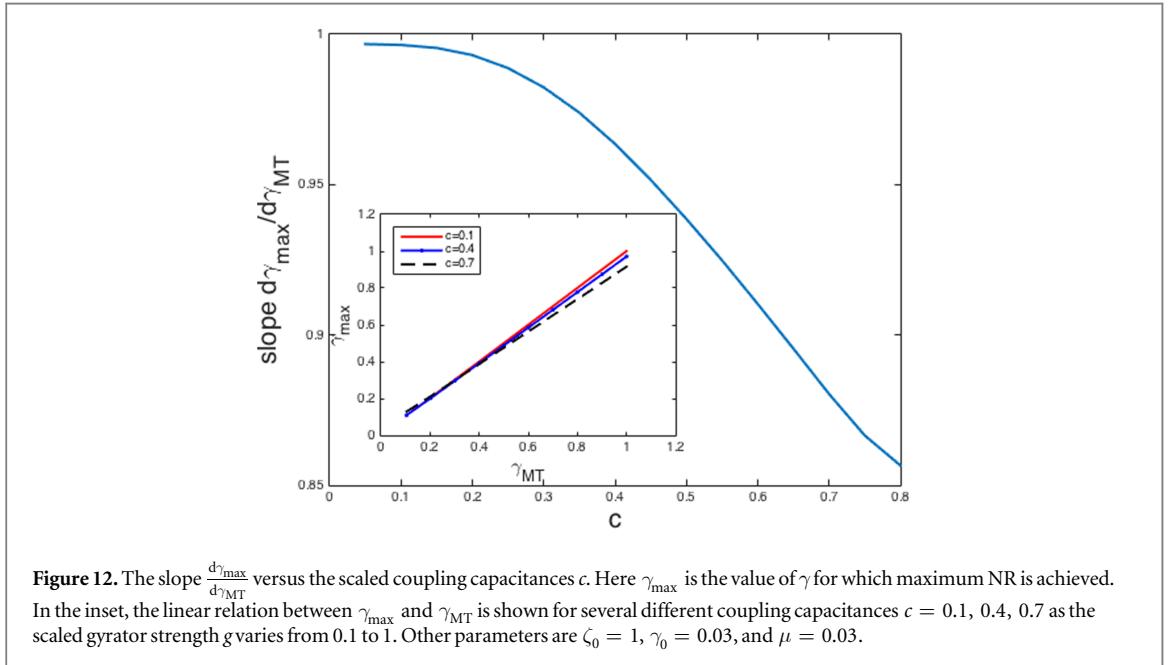
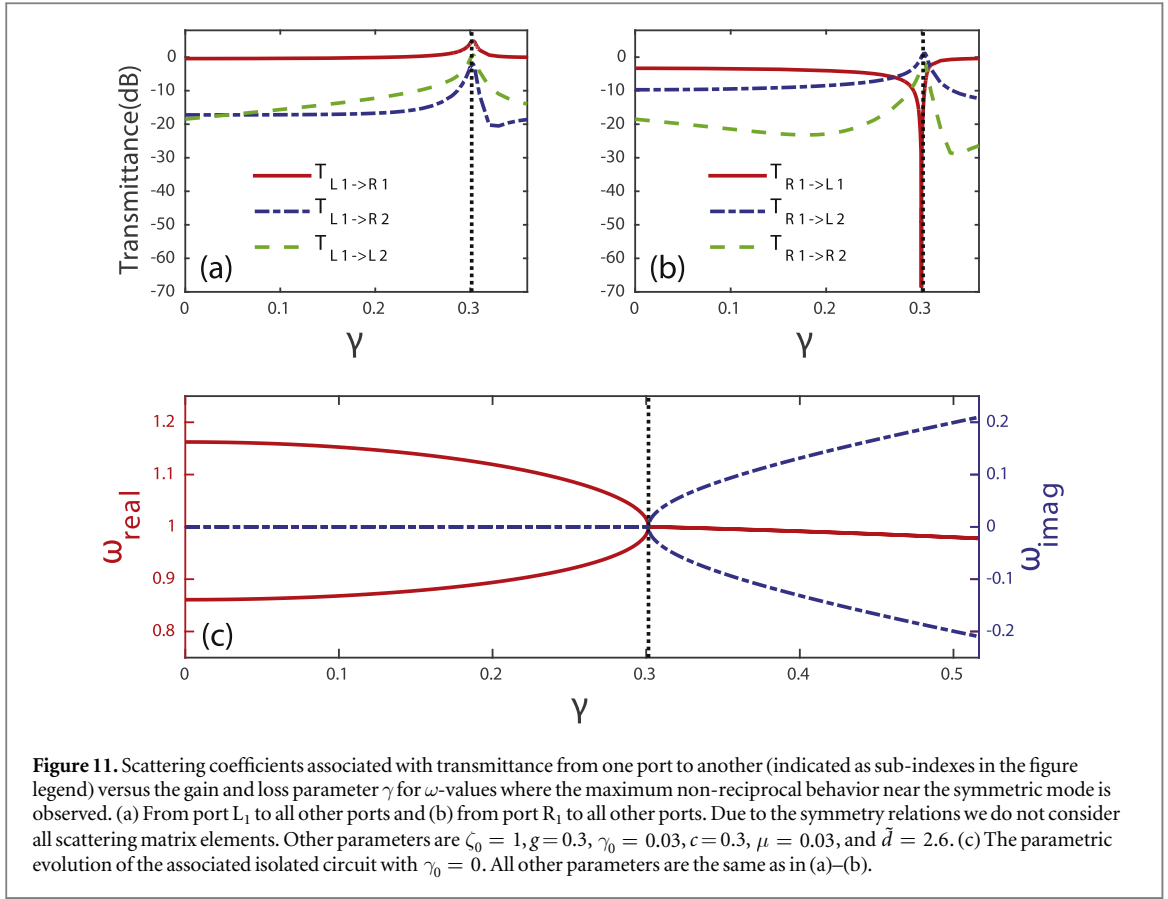
where $\mathcal{T}_{L_1 \rightarrow R_1} = |S_{11}^{\text{oi}}(2,1)|^2$ denotes the transmission coefficient from the L_1 port to R_1 port and $\mathcal{T}_{R_1 \rightarrow L_1} = |S_{11}^{\text{oi}}(1, 2)|^2$ denotes the transmission coefficient in the reverse direction, expresses the nonreciprocity between the two ports of the top transmission line. Note that \max_{ω} refers to the the maximum of this quantity as a function of frequency for all other parameters fixed.

This completes the description of the four-port device in terms of its scattering matrix, as parameterized through a lumped-element model of the coupled microstrip resonator pair.

3.5. Giant intra-guide non-reciprocity and inter-guide transmittance

The COMSOL simulation presented in section 2.2 indicated that our four-port $\mathcal{M}\mathcal{T}$ -symmetric photonic structure demonstrates strong non-reciprocal intra-guide transport and an enhanced inter-guide transmittance for a value of the gain and loss parameter close to $\gamma \approx \gamma_{\mathcal{M}\mathcal{T}}$. However, the complexity of the electromagnetic problem—involving many parameters—was not allowing for a thorough analytical or even numerical investigation of the properties of the set-up. In contrast, the equivalent lumped circuit, is not only very transparent but it also provides a very attractive framework where detailed numerical and analytical investigations can be performed.

First we demonstrate that the giant intra-guide non-reciprocal behavior and inter-guide transmittance at $\gamma \approx \gamma_{\mathcal{M}\mathcal{T}}$ is a universal phenomenon and, as such, it pertains also to the transport characteristics of the lump circuit. Our investigation of the electronic model focuses on the frequency region near the symmetric-mode resonance, where the intra-guide non-reciprocity NR describing the R_1 to L_1 port isolation, see equation (21), is typically experiencing its maximum value. This can be seen in figures 11(a), (b) where we observe that the non-reciprocity between L_1 and R_1 take values $\text{NR} \sim 80$ dBs while the transmittance between L_1 and other ports



(R_2, L_2) is $T_{L_1 \rightarrow L_2} \sim T_{L_1 \rightarrow R_2} \sim 0$ dBs at $\gamma \sim \gamma_{MT}$. The latter can be evaluated from the parametric evolution of the eigen-frequencies equation (6) of the corresponding isolated system, see figure 11(c).

In figure 12 we show the dependence of the isolation properties, between intra-guide ports, on the resonator coupling strength to the transmission lines. The inset illustrates that the position of the maximum NR, denoted by γ_{\max} , is always slightly below the MT EP, consistent with the above discussion, with a linear relationship. The main figure shows the slope of this linear relation. Deviating only slightly from unity as the coupling increases, this shows that the coupling strength is not very important.

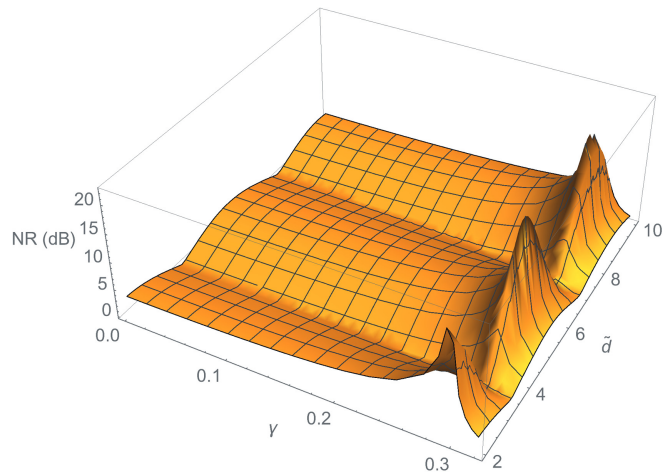


Figure 13. A 3D plot of nonreciprocity parameter NR versus gain/loss parameter γ and the scaled distance \tilde{d} . Other parameters are as in figure 11 i.e. $\zeta_0 = 1, g = 0.3, \gamma_0 = 0.03, c = 0.3,$ and $\mu = 0.03$. The value of $\gamma_{\mathcal{MT}}$ for the corresponding isolated system is $\gamma_{\mathcal{MT}} = 0.3$ (see figure 11). Notice also that for smaller values of $\gamma < \gamma_{\mathcal{MT}}$ we have a weak non-reciprocal behavior, and that the preferred transmittance direction alternates for each domain $n\pi < \tilde{d} < (n + 1)\pi$.

Finally in figure 13 we report our results for NR as a function of the gain/loss parameter γ and the coupling phase delay \tilde{d} . The latter defines the scaled distance between the coupling points of the two circuit elements along the transmission line. Note first that the behavior of NR versus \tilde{d} is periodic with a period π and maxima near the $1/4$ wave positions. Specifically we have that $\tilde{d}_{\max} = \left(\frac{n}{2} + \frac{1}{4}\right)2\pi$. This condition is expected due to the important role that impedance matching between the respective coupling points play in the conditions to achieve a maximum NR. The sharp increase in the NR with the gain/loss parameter γ reflects the crucial role that both the gyrotropy of the inter-resonator coupling and the \mathcal{MT} EP behavior have in enabling the non-reciprocity: as discussed in section 3.2, the mode coalescence occurring in the neighborhood of $\gamma_{\mathcal{MT}}$ (see figure 10) has two important consequences. Firstly, it brings the symmetric and antisymmetric frequencies together. As a result, the incident signal significantly excites both modes simultaneously. Secondly, it allows a gyro-tropically driven non-reciprocal response, provided that the phase relation between the driven modes has a significant quadrature component. This is assured by the presence of the weak intrinsic dissipation γ_0 and the novel \mathcal{MT} phaser coalescence near the EP. We note that in our four port device, this weak dissipation can be effectively provided by radiative coupling into the second transmission line.

4. Conclusions

We have analyzed the transport properties of a mirror-symmetric photonic circuit consisting of two resonators—one with gain and the other one with equal amount of loss. The photonic structure is placed on top of a gyrotropic substrate and it is coupled together and with two bus waveguides. Via numerical simulations in the microwave domain we were able to demonstrate that the system shows anomalous transport properties: strong intra-guide non-reciprocal transport and inter-guide enhanced transmittance. These features are universal and can be explained using an equivalent lump circuit. The latter allows for an exact theoretical description while due to its relative simplicity, it offers new insights in the anomalous transport properties of the photonic circuit. Using this framework we find that the origin of the anomalous transport is associated with the interplay of an EP degeneracy with the gyrotropy. Our results might find application to reconfigurable beam splitters, buffers and tunable isolators relevant to communication systems design.

Acknowledgments

This work was partly sponsored by an AFOSR MURI Grant No. FA9550-14-1-0037, and by an NSF Grant No. DMR-1306984.

References

- [1] Makris K G et al 2008 *Phys. Rev. Lett.* **100** 103904

- [2] Rüter C E et al 2010 *Nat. Phys.* **6** 192
Guo A et al 2009 *Phys. Rev. Lett.* **103** 093902
- [3] Feng L et al 2011 *Science* **333** 729
- [4] Regensburger A, Bersch C, Miri M A, Onishchukov G, Christodoulides D N and Peschel U 2012 *Nature* **488** 167
- [5] Chang L et al 2014 *Nat. Photon.* **8** 524
- [6] Peng B et al 2014 *Nat. Phys.* **10** 394
- [7] Hodaei H et al 2014 *Science* **346** 975
Feng L et al 2014 *Science* **346** 972
- [8] Lin Z, Ramezani H, Eichelkraut T, Kottos T, Cao H and Christodoulides D N 2011 *Phys. Rev. Lett.* **106** 213901
- [9] Longhi S 2009 *Phys. Rev. Lett.* **103** 123601
- [10] Bender N, Li H, Ellis F M and Kottos T 2015 *Phys. Rev. A* **92** 041803(R)
- [11] Zheng M C et al 2010 *Phys. Rev. A* **82** 010103
- [12] Ramezani H, Kottos T, El-Ganaïny R and Christodoulides D N 2010 *Phys. Rev. A* **82** 043803
- [13] Bender N, Factor S, Bodyfelt J D, Ramezani H, Christodoulides D N, Ellis F M and Kottos T 2013 *Phys. Rev. Lett.* **110** 234101
- [14] Ramezani H et al 2012 *Opt. Express* **20** 26200
- [15] Longhi S 2010 *Phys. Rev. A* **82** 031801
Chong Y D et al 2011 *Phys. Rev. Lett.* **106** 093902
- [16] Ramezani H, Christodoulides D N, Kovanis V, Vitebskiy I and Kottos T 2012 *Phys. Rev. Lett.* **109** 033902
- [17] Peng B, Ozdemir S K, Rotter S, Yilmaz H, Liertzer M, Monifi F, Bender C M, Nori F and Yang L 2014 *Science* **346** 328
- [18] Chitsazi M, Factor S, Schindler J, Ramezani H, Ellis F M and Kottos T 2014 *Phys. Rev. A* **89** 043842
- [19] El-Ganaïny R, Khajavikhan M and Ge L 2014 *Phys. Rev. A* **90** 013802
- [20] Lee J M, Factor S, Lin Z, Vitebskiy I, Ellis F M and Kottos T 2014 *Phys. Rev. Lett.* **112** 253902
- [21] Schindler J, Lin Z, Lee J M, Ramezani H, Ellis F M and Kottos T 2012 *J. Phys. A: Math. Theor.* **45** 444029
- [22] Zhong-Peng L, Jing Z, Şahin K Ö, Bo P, Hui J, Xin-You L, Chun-Wen L, Lan Y, Franco N and Yu-xi L 2015 arXiv:1510.05249
- [23] Schomerus H 2013 *Phil. Trans. R. Soc. A* **371** 20120194
- [24] Thomas R, Li H, Ellis F M and Kottos T 2015 submitted
- [25] El-Ganaïny R, Eisfeld A, Levy M and Christodoulides D N 2013 *Appl. Phys. Lett.* **103** 161105
- [26] Sounas D L, Caloz C and Alú A 2013 *Nat. Commun.* **4** 2407
- [27] Yu Z and Fan S 2009 *Nat. Photon.* **3** 91
- [28] Lira H, Yu Z, Fan S and Lipson M 2012 *Phys. Rev. Lett.* **109** 033901
- [29] Leach J H, Liu H, Avrutin V, Rowe E, Ozgur U, Morkoc H, Song Y-Y and Wu M 2010 *J. Appl. Phys.* **108** 064106
- [30] Bender C M and Boettcher S 1998 *Phys. Rev. Lett.* **80** 5243
Bender C M 2007 *Rep. Prog. Phys.* **70** 947
- [31] COMSOL Multiphysics v. 5.2. www.comsol.com. COMSOL AB, Stockholm, Sweden
- [32] Laha S, Kaya S, Kodi A and Matolak D 2012 Double gate MOSFET based efficient wide band tunable power amplifiers 2012 *IEEE XIII Annual Wireless and Microwave Technology Conference (WAMICON)* p 1–4